RSC Advances

PAPER

View Article Online
View Journal | View Issue

Cite this: *RSC Adv.*, 2019, **9**, 21601

Aspect ratio-controlled preparation of α-$CaSO_4 \cdot 0.5H_2O$ from phosphogypsum in potassium tartrate aqueous solution†

Xiangbin Sun,[a] Genlei Zhang *[ab] and Peng Cui*[a]

Received 12th May 2019
Accepted 28th June 2019

DOI: 10.1039/c9ra03569a

rsc.li/rsc-advances

In this study, a simple and efficient strategy is developed to synthesize rod-shaped α-$CaSO_4 \cdot 0.5H_2O$ crystals with tunable aspect ratio from industrial phosphogypsum only in potassium tartrate aqueous solution at a low temperature. Industrial phosphogypsum can be effectively converted into rod-shaped α-$CaSO_4 \cdot 0.5H_2O$ crystals with the assistance of potassium tartrate, and the aspect ratio of α-$CaSO_4 \cdot 0.5H_2O$ crystals gradually decreases from 52 : 1 to 1 : 1 with increasing the concentration of potassium tartrate. The formation process of the rod-shaped α-$CaSO_4 \cdot 0.5H_2O$ crystals in this system involves the dissolution of $CaSO_4 \cdot 2H_2O$ and nucleation of α-$CaSO_4 \cdot 0.5H_2O$ crystals. The tartrate ions from potassium tartrate in this system preferentially bind to (001) and (002) facets of α-$CaSO_4 \cdot 0.5H_2O$ crystals, inhibiting the growth of α-$CaSO_4 \cdot 0.5H_2O$ crystals along the *c*-axis and controlling its morphology and aspect ratio.

1 Introduction

Industrial phosphogypsum (I-PG) is mainly composed of calcium sulfate dihydrate ($CaSO_4 \cdot 2H_2O$) and it is the main byproduct of the production process of phosphoric acid.[1–3] Annual emissions of I-PG around the world have exceeded one billion tons over the last three years and the huge amount of I-PG not only occupies farmland but also causes severe pollution of the surrounding environment.[3] In recent years, high-value utilization of I-PG has drawn significant attention and so far, the most effective way to achieve high-value utilization of I-PG is to produce α-calcium sulphate hemihydrate (α-$CaSO_4 \cdot 0.5H_2O$).[4–6]

To date, methods for preparing α-$CaSO_4 \cdot 0.5H_2O$ crystals from $CaSO_4 \cdot 2H_2O$ mainly include autoclave hydrothermal,[7–10] atmospheric salt solution,[11–14] reverse microemulsion[15] and alcohol–water solution.[16–18] The autoclave hydrothermal method involves high temperature (usually above 120 °C) and certain pressure,[19,20] which are not conducive to industrialization. Whereas the crystallization temperature of α-$CaSO_4 \cdot 0.5H_2O$ crystals can be significantly decreased in salt solutions with high concentration by atmospheric salt solution method.[21–23] However, the high-concentration salt solutions can lead to serious equipment corrosion.[24,25] The reverse microemulsion and alcohol–water strategies that require a large amount of surfactants such as CTAB, SDS and organic alcohols such as ethylene glycol and glycerine.[26,27] Although these surfactants and organic alcohols are advantageous for the synthesis of α-$CaSO_4 \cdot 0.5H_2O$ crystals with various morphologies and sizes, the close adsorptions to the surface of α-$CaSO_4 \cdot 0.5H_2O$ crystals cause great trouble for subsequent separation and cleaning. Therefore, the exploration of simple, low-cost and environmentally friendly crystal transformation method is one of the research hotspots of the high-value utilization of I-PG.

The prepared α-$CaSO_4 \cdot 0.5H_2O$ crystals are wildly used in construction industry, special binder, 3D print and medical materials.[28–39] Mechanical strength is one of the most important properties for α-$CaSO_4 \cdot 0.5H_2O$ crystals that we pay more attention to, which is closely related to the crystal morphology.[40,41] Presently, other crystal structures of α-$CaSO_4 \cdot 0.5H_2O$ crystals besides 1D structure have rarely been reported.[4] And the 1D α-$CaSO_4 \cdot 0.5H_2O$ crystals with a lower aspect ratio (length-to-diameter) have better mechanical strength than these with higher one.[42] To control the aspect ratio of 1D α-$CaSO_4 \cdot 0.5H_2O$ crystals, various crystallization (synthetic) methods have been proposed.[43,44] The α-$CaSO_4 \cdot 0.5H_2O$ whiskers can be obtained by autoclave hydrothermal method in the presence of Mg^{2+}, but its aspect ratio cannot be efficiently controlled and the reaction temperature up to 150 °C.[9,18] Rod-shaped α-$CaSO_4 \cdot 0.5H_2O$ crystals were successfully produced from flue gas desulfurization in $Ca(NO_3)_2$ solution and its size could be significantly controlled *via* adjusting

[a]*School of Chemistry and Chemical Engineering, Anhui Province Key Laboratory of Controllable Chemistry Reaction and Material Chemical Engineering, Hefei University of Technology, Tunxi Road 193, Hefei 230009, PR China. E-mail: genleizhang@hfut.edu.cn; cuipeng@hfut.edu.cn*

[b]*School of Materials Science and Engineering, Hefei University of Technology, Tunxi Road 193, Hefei 230009, PR China*

† Electronic supplementary information (ESI) available. See DOI: 10.1039/c9ra03569a

the $Ca(NO_3)_2$ concentration.[42] However, regardless of the size of the rod-shaped α-$CaSO_4 \cdot 0.5H_2O$ crystals, its aspect ratio remained unchanged. Although $CaSO_4 \cdot 2H_2O$ crystals can be easily converted into α-$CaSO_4 \cdot 0.5H_2O$ crystals with 1D structure in many inorganic salt systems, the aspect ratio of the obtained α-$CaSO_4 \cdot 0.5H_2O$ crystals cannot be effectively regulated without any other organic modifiers. Using organic acid as the modifiers, rod-shaped α-$CaSO_4 \cdot 0.5H_2O$ crystals with different aspect ratios were successfully synthesized in $CaCl_2$ aqueous solution containing a large amount of glycerol.[14,45] What is more, α-$CaSO_4 \cdot 0.5H_2O$ crystals having a controlled aspect ratio was obtained employing surfactants such as CTAB and SDS as modifiers.[15,27] However, the adjustable range of the aspect ratio is small, and the use of a large amount of surfactants brings great difficulty to the subsequent cleaning and purification work.

In this study, a simple, eco-friendly, and efficient route was developed to synthesize rod-shaped α-$CaSO_4 \cdot 0.5H_2O$ crystals with different aspect ratios in potassium tartrate (PT) aqueous solution. The conversion process and mechanism of the rod-shaped α-$CaSO_4 \cdot 0.5H_2O$ crystals were investigated. The selective use of PT was demonstrated to be vital for the aspect ratio of the obtained rod-shaped α-$CaSO_4 \cdot 0.5H_2O$ crystals, and as its concentration increased, the aspect ratio of α-$CaSO_4 \cdot 0.5H_2O$ crystals gradually decreased. The preferential adsorption of PT on the (001) and (002) facets of the obtained α-$CaSO_4 \cdot 0.5H_2O$ crystals inhibited the growth of the crystal along the *c*-axis, and thereby realized the control of the aspect ratio.

2 Experimental

2.1 Materials

The I-PG was obtained from Anhui Liuguo Chemical Co. Ltd, Anhui Province, China. Analytical reagent grade of sulfuric acid (H_2SO_4), potassium tartrate (PT) and ethanol were all purchased from Sinopharm Chemical Reagent Co., Ltd., Shanghai, China. PT aqueous solutions with different PT concentrations were prepared using purified water.

2.2 Preparation of rod-shaped α-$CaSO_4 \cdot 0.5H_2O$ crystals

Pretreatment of I-PG. 50 g of the I-PG was initially immersed in 100 mL of 1 M H_2SO_4 aqueous solution at 80 °C for 1 h. After the solution was then cooled down to room temperature, the grayish white precipitate was collected by repeated centrifugation and washed with purified water to obtain the H_2SO_4-treated I-PG.

Preparation of the rod-shaped α-$CaSO_4 \cdot 0.5H_2O$ crystals. 40 mL of 50 mM PT aqueous solution was first added into a 250 mL three-necked flask equipped with a reflux condenser and preheated to 90 °C in an oil bath. Then, 10 g of the H_2SO_4-treated I-PG obtained in the above experimental procedure was added into the three-necked flask under stirring at a constant rate of 100 rpm, and followed with continuous heating to 98 °C. The mixed solution was kept at 98 °C for 6 h while stirring was constant. After the completion of the reaction, the slurry was withdrawn and filtrated immediately, washed with purified water and absolute ethanol before drying at 60 °C for 4 h in an oven. For comparison, different samples were prepared in the same procedure with different PT concentrations (20 mM, 100 mM and 200 mM) and reaction times (0.5 h, 1 h, 2 h and 4 h).

2.3 Characterizations

The X-ray fluorescence spectroscopy (XRF) used in this study was consisted of a 40 kV X-ray tube with a Rh anode target excitation source (Shimadzu; Japan). The scanning electronic microscopy (SEM) images were taken out by using a SU8020 scanning electron microscope (Hitachi; Japan) with an accelerating voltage of 10 kV. The transmission electron microscopy (TEM) and high-resolution TEM (HRTEM) equipped with selected area electron diffraction (SAED) were performed using JEOL 2100F microscope (JEOL; Japan) operated at 200 kV. The energy dispersive X-ray spectroscopy (EDS) analysis was conducted using the TEM to identify the elemental composition of samples. The X-ray diffraction (XRD) spectra were operated *via* a Rigaku D/Max-2500 X-ray diffractometer (Rigaku; Japan) with a Cu Kα radiation ($\lambda = 0.15406$ nm) operated at 40 kV and 80 mA. The thermogravimetry and differential scanning calorimetry (TG-DSC) were conducted at a heating rate of 10°C min^{-1} (NET-ZSCH; Germany) to distinguish α-$CaSO_4 \cdot 0.5H_2O$ from the hemihydrate phase. The Fourier transform infrared spectroscopy (FT-IR) were recorded on (LX10-8813; USA) FT-IR spectrometer under the transmission scheme by using the KBr pellet technique. The X-ray photoelectron spectroscopy (XPS) data were recorded by ESCALAB250Xi (Thermo Scientific; USA) with using a monochromatized Al Kα ($h = 1486.6$ eV) X-ray source. All the spectra were corrected using C 1s signal located at 284.70 eV.

3 Results and discussion

The I-PG from Liuguo Chemical Co., Ltd. is mainly composed of prismatic-sheet crystals with a width of 40–60 μm and a length of 80–120 μm, and its scanning electronic microscopy (SEM) images are shown in Fig. 1a. In addition, a large amount of fine debris was covered on the prismatic-sheet structure, and many impurity elements in the I-PG were detected by X-ray fluorescence spectroscopy (XRF) and the result was recorded in Table S1.† Fortunately, the fine debris and impurity elements in the I-PG could be effectively removed by H_2SO_4 aqueous solution while the structure and size of the prismatic-sheet crystals remained almost unchanged, which were demonstrated by SEM, transmission electron microscopic (TEM) and energy dispersive X-ray spectroscopy (EDS), and the results shown in Fig. 1b, c and S1,† respectively. To further characterize the H_2SO_4-treated I-PG, we used a number of tools to analyze the elemental distribution of the crystal and identify the structure. The EDS elemental mapping images of the obtained H_2SO_4-treated I-PG (Fig. 1d) confirmed that Ca, S and O were homogeneously distributed throughout the prismatic-sheet crystal. The high-resolution TEM (HRTEM) image of the obtained H_2SO_4-treated I-PG (Fig. 1e) showed that the observed *d*-spacing measured from the prismatic-sheet crystal was 0.763 nm, which

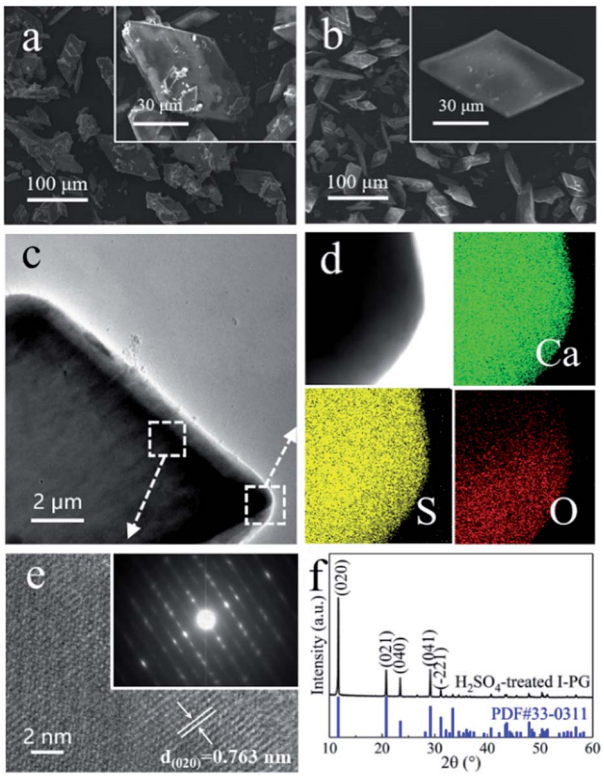

Fig. 1 (a) SEM image of I-PG; (b) SEM and (c) TEM images of the H_2SO_4-treated I-PG, and (d) the corresponding elemental mapping images showing the distribution of Ca, S and O; (e) HRTEM and SAED (inset) images and (f) XRD pattern of the H_2SO_4-treated I-PG.

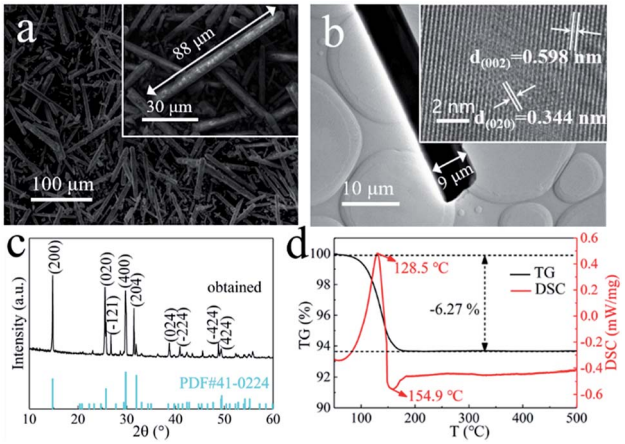

Fig. 2 (a) SEM and (b) TEM images of the α-$CaSO_4 \cdot 0.5H_2O$ crystals prepared in 50 mM PT aqueous solution for 6 h; (c) XRD pattern and (d) TG-DSC analysis of the obtained α-$CaSO_4 \cdot 0.5H_2O$ crystals. The inset images in (b) show the corresponding HRTEM image of obtained crystal.

was close to that for the (020) facet of the $CaSO_4 \cdot 2H_2O$ crystals.[46] The corresponding selected area electron diffraction (SAED) image (inset in Fig. 1e) implied that the prismatic-sheet crystals possess a special single-crystalline feature. The X-ray diffraction (XRD) pattern of the obtained H_2SO_4-treated I-PG was shown in Fig. 1f, and the main diffraction peaks at 11.66°, 20.78°, 23.41°, 29.14° and 31.18° were assigned to $CaSO_4 \cdot 2H_2O$ (020), (021), (040), (041) and (−221) facets (JCPDS 33-0311),[8] respectively. Furthermore, its thermogravimetry and differential scanning calorimetry (TG-DSC) analysis result (Fig. S2†) indicated that the thermal stability of the H_2SO_4-treated I-PG was the same as that of $CaSO_4 \cdot 2H_2O$ crystals.[20] The above characterization results indicated that the obtained H_2SO_4-treated I-PG was $CaSO_4 \cdot 2H_2O$ crystals with prismatic-sheet structure.[13]

The morphology of the obtained crystals prepared from the H_2SO_4-treated I-PG that used PT as the inducer was initially determined by electron microscopy. Typical SEM and TEM images of the crystals prepared in 50 mM PT aqueous solution for 6 h are shown in Fig. 2a and b. The SEM image (Fig. 2a) showed that the product consists of uniform rod-shaped crystals with a yield approaching 100%. The average length of the as-prepared rod-shaped crystals is about 88 μm (Fig. 2a) with a width of about 9 μm (Fig. 2b), that is, its aspect ratio is about 10 : 1. The HRTEM image (inset in Fig. 2b) of the crystal showed that the observed *d*-spacing were 0.598 nm and 0.344 nm, closing to that for (002) and (020) facets of α-$CaSO_4 \cdot 0.5H_2O$, respectively.[44] The XRD pattern of the as-prepared rod-shaped crystals was shown in Fig. 2c, and the main diffraction peaks at 14.91°, 25.61°, 26.82°, 29.77° and 31.52° were assigned to (200), (020), (−121), (400) and (204) facets of $CaSO_4 \cdot 0.5H_2O$ crystals (JCPDS 41-0224), respectively.[41] The thermogravimetry and differential scanning calorimetry (TG-DSC) analysis of the obtained rod-shaped crystals was shown in Fig. 2d. The TG curve of the as-prepared rod-shaped crystals showed a 6.27% weight loss between 100 °C and 500 °C, which is consistent with the H_2O mass fraction in $CaSO_4 \cdot 0.5H_2O$ crystals.[5] Moreover, the endothermic peak appearing at 128.5 °C on the DSC curve also confirmed that the as-prepared crystals may be composed of $CaSO_4 \cdot 0.5H_2O$ crystals.[20] The XRD and TG-DSC results indicate that the as-prepared rod-shaped crystals are $CaSO_4 \cdot 0.5H_2O$ crystals. It is well known that there are two types of $CaSO_4 \cdot 0.5H_2O$ crystals, namely α-$CaSO_4 \cdot 0.5H_2O$ and β-$CaSO_4 \cdot 0.5H_2O$, and an exothermic peak at 154.9 °C on the DSC curve indicates that the as-prepared $CaSO_4 \cdot 0.5H_2O$ crystals are α-$CaSO_4 \cdot 0.5H_2O$ crystals.[4,47]

To gain in-depth understanding of the conversion mechanism of the prismatic-sheet $CaSO_4 \cdot 2H_2O$ crystals to rod-shaped α-$CaSO_4 \cdot 0.5H_2O$ crystals, the conversion process was carefully investigated by collecting the SEM images (Fig. 3) of the intermediates at different reaction time. As shown in Fig. 3a of the intermediates obtained after the 0.5 h synthesis, a large amount of convex/concave regions (the yellow dotted area in Fig. 3a) and small particles (the yellow circles in Fig. 3a) with the diameter of less than 0.2 μm on the surface of the prismatic-sheet crystals could be observed. The XRD information of the intermediate (the black spectrum in Fig. 3e) indicated that the dissolution and nucleation behaviors of $CaSO_4 \cdot 2H_2O$ crystals occurred at this stage. As the reaction prolonged to 1 h, small particles with the diameter of less than 3 μm and a small proportion of short rod crystals appeared at the convex/concave regions (Fig. 3b). And at this point, it was learned from the XRD pattern (the purple spectrum in Fig. 3e) that part of the $CaSO_4 \cdot 2H_2O$ crystals

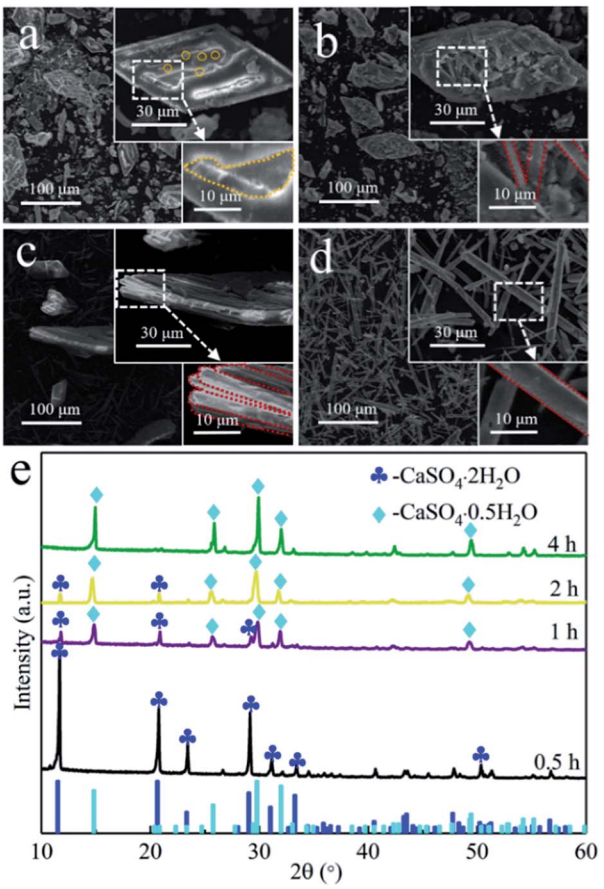

Fig. 3 SEM images of the intermediates of rod-shaped α-$CaSO_4$·0.5H_2O crystals intermediates obtained after proceeding the reaction for (a) 0.5, (b) 1, (c) 2, and (d) 4 h; (e) XRD patterns of corresponding intermediates.

has been converted to α-$CaSO_4$·0.5H_2O crystals. When the reaction time proceeded to 2 h, the initial prismatic-sheet $CaSO_4$·2H_2O crystals were entirely consisted with rod-shaped crystals (Fig. 3c), and this intermediate is mostly consisted of α-$CaSO_4$·0.5H_2O crystals (the yellow XRD spectrum in Fig. 3e). Further extension of reaction time to 4 h, the rod crystals in Fig. 3c were detached from its nucleation region and eventually evolved into a structurally intact uniform rod-shaped α-$CaSO_4$·0.5H_2O crystals (Fig. 3d and the green XRD spectrum in Fig. 3e). This time-dependent morphological changes suggest an attached process of the formation of rod-shaped α-$CaSO_4$·0.5H_2O crystals, where it started from the dissolution of the $CaSO_4$·2H_2O crystals and the initial form of small particles, then gradually grew into short rod-shaped crystals and finally lead to the uniform rod-shaped α-$CaSO_4$·0.5H_2O crystals (Fig. 2a).

In this study, the prismatic-sheet $CaSO_4$·2H_2O crystals was successfully converted into rod-shaped α-$CaSO_4$·0.5H_2O crystals in PT aqueous solution. However, we found that there were no changes on the morphology and physicochemical properties of the prismatic-sheet $CaSO_4$·2H_2O crystals when the PT was absent, and as shown in Fig. 4a and the XRD pattern in Fig. 4f. That is, the PT used as crystallize modifier in the formation of rod-shaped α-$CaSO_4$·0.5H_2O crystals. As combining indicated by Fig. 4b and f, the yield of the rod-shaped α-$CaSO_4$·0.5H_2O crystals increased substantially when the PT was present. Surprisingly, the length and aspect ratio of the rod-shaped α-$CaSO_4$·0.5H_2O crystals were depended on the concentration of PT, as shown in Fig. 4b–e, when the concentrations of PT were 20 mM, 50 mM, 100 mM and 200 mM, respectively, the lengths of the obtained rod-shaped α-$CaSO_4$·0.5H_2O crystals were 105 μm, 88 μm, 33 μm and 21 μm, and the corresponding widths were 2 μm, 9 μm, 11 μm and 20 μm in turn. That is, the aspect ratios of the rod-shaped ones were about 52 : 1, 10 : 1, 3 : 1 and 1 : 1, respectively (Fig. S3†). In addition, the rod-shaped α-$CaSO_4$·0.5H_2O crystals also could be obtained while used NaCl instead of PT, but its aspect ratio could not be effectively regulated *via* the concentration of NaCl (Fig. S4 and S5†). The EDS elemental mapping images of the obtained rod-shaped α-$CaSO_4$·0.5H_2O crystals (Fig. 5a) confirmed that carbonaceous species were adsorbed onto the surface of the α-$CaSO_4$·0.5H_2O crystals, which was also confirmed by the difference between the fourier transform infrared spectroscopy (FT-IR) spectra of the pure α-$CaSO_4$·0.5H_2O crystals and the obtained rod-shaped α-$CaSO_4$·0.5H_2O crystals in this work (Fig. 5b). As shown in Fig. 5b, three adsorption peaks at 1584 cm^{-1}, 1404 cm^{-1} and 1385 cm^{-1} in the FT-IR spectrum of the obtained α-$CaSO_4$·0.5H_2O crystals (blue curve in Fig. 5b) should be assigned to the asymmetric and symmetric stretching vibrations of –COO–,[44,48] and the three peaks were all shifted to lower wavenumbers as compared with those in the FT-IR spectrum of PT. This result indicated that tartrate ions from PT were

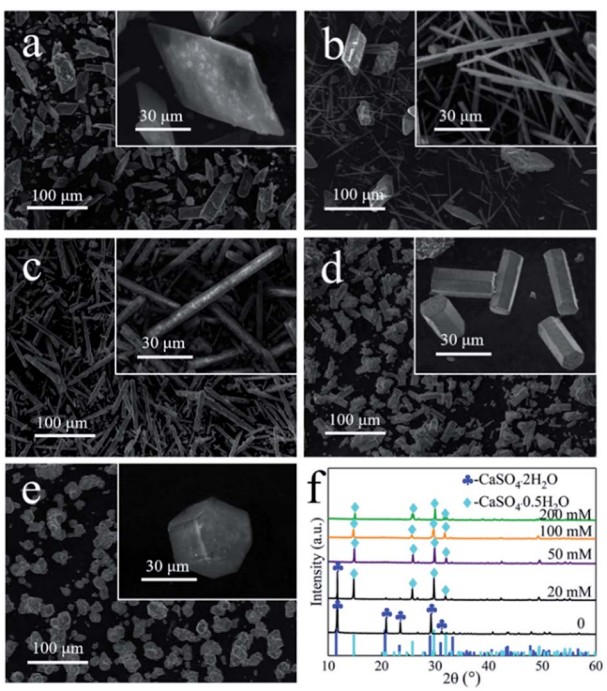

Fig. 4 SEM images of samples that prepared in PT aqueous solution with different PT concentrations: (a) 0 mM, (b) 20 mM, (c) 50 mM, (d) 100 mM and (e) 200 mM; (f) XRD patterns of the corresponding samples.

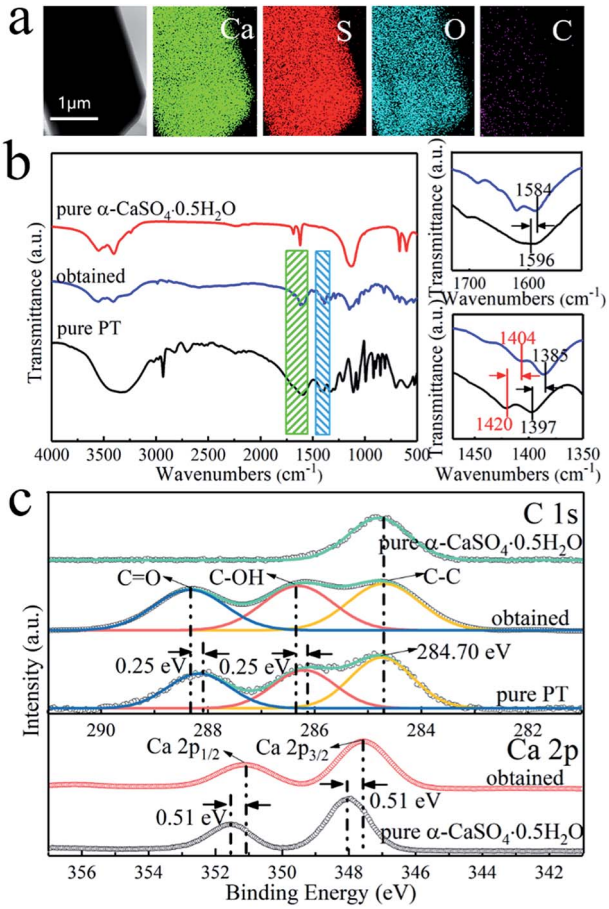

Fig. 5 (a) Elemental mapping images of the obtained rod-shaped α-$CaSO_4 \cdot 0.5H_2O$ crystals prepared in 50 mM PT aqueous solution; (b) FT-IR spectra of PT, pure α-$CaSO_4 \cdot 0.5H_2O$ crystals and the obtained crystals; (c) C 1s and Ca 2p XPS spectra of PT, pure α-$CaSO_4 \cdot 0.5H_2O$ and obtained crystals.

absorbed on the surface of the obtained α-$CaSO_4 \cdot 0.5H_2O$ crystals. The adsorption behavior of PT was also illustrated by X-ray photoelectron spectroscopy (XPS). Compared to the C 1s XPS spectrum of pure α-$CaSO_4 \cdot 0.5H_2O$ in Fig. 5c, two new signal peaks appeared at around 288.41 eV and 286.41 eV in the C 1s XPS spectrum of the obtained α-$CaSO_4 \cdot 0.5H_2O$ crystals, which should be assigned to the C=O and C–OH groups.[14] This clearly indicated the adsorption of PT on the obtained α-$CaSO_4 \cdot 0.5H_2O$ surfaces considering the similarity of the C 1s XPS spectra of the obtained α-$CaSO_4 \cdot 0.5H_2O$ and PT. However, the C 1s peaks of C=O and C–OH groups in the obtained α-$CaSO_4 \cdot 0.5H_2O$ were positively shifted about 0.25 eV as compared with that in PT, implying that the existence of the electronic effect between tartrate groups and Ca atoms.[49–51] Furthermore, this speculate was also determined by the negative shift of the Ca 2p XPS peaks of the obtained α-$CaSO_4 \cdot 0.5H_2O$ comparing to that of the pure α-$CaSO_4 \cdot 0.5H_2O$ in Fig. 5c.[52–54] One of the reasons for the dependence of the aspect ratio of the rod-shaped α-$CaSO_4 \cdot 0.5H_2O$ crystals on PT may be related to the preferential adsorption of PT on the crystal surfaces, which is caused by the difference in the properties of the rod-shaped α-$CaSO_4 \cdot 0.5H_2O$ facets.

The molecular structure of the rod-shaped α-$CaSO_4 \cdot 0.5H_2O$ crystals deduced by Material Studio 5.0 software[55] was shown in Fig. 6. The 3D model of the α-$CaSO_4 \cdot 0.5H_2O$ along the *c*-axis direction in Fig. 6a was derived a $2 \times 2 \times 2$ supercell molecular structure model ($a = 12.0275$ Å, $b = 6.9312$ Å, $c = 12.6919$ Å), while the facet models in Fig. 6b–d were the top-view charts of (001), (002), (200), (400), (020), and (020) facets cut from the 3D model, ignoring the thickness of the facets. The 3D model in Fig. 6a showed that the obtained rod-shaped α-$CaSO_4 \cdot 0.5H_2O$ was consisted of –Ca–SO_4–Ca–SO_4–Ca– chains (partial structure of –Ca–SO_4–Ca– chain in Fig. S6†), where every S atom was covalently bonded to the four O atoms. The distribution of Ca, S, O and H on different facets of the rod-shaped α-$CaSO_4 \cdot 0.5H_2O$ crystals were displayed in Fig. 6b–d, and the corresponding statistical results were listed in Table 1. The data in Table 1 showed that the distribution densities of Ca atoms on (001), (002), (200), (400) and (020) facets were 0.0900, 0.0900, 0.0568, 0.0568, and 0.0066, respectively. The denser distribution of Ca atoms on the top facets as (001) and (002) than that on the side facets as (200), (400) and (020) indicated that tartrate ions would preferentially adsorb on top facets of the rod-shaped α-$CaSO_4 \cdot 0.5H_2O$ crystals, which is further demonstrated by the C element content of the side and top facets of α-$CaSO_4 \cdot 0.5H_2O$ crystals (Fig. S7†). The preferential adsorption of tartrate ions reduced the specific surface energy of (001) and (002) facets, and led to an increased exposure of the two facets in the rod-shaped α-$CaSO_4 \cdot 0.5H_2O$ crystals, which hindered the crystal growth along the *c*-axis and reduced the exposure of (200), (400) and (020) side facets.[12] Consequently, the length and width of the α-$CaSO_4 \cdot 0.5H_2O$ crystals gradually decreased and increased as the concentration of PT increased, respectively. Hence, using PT

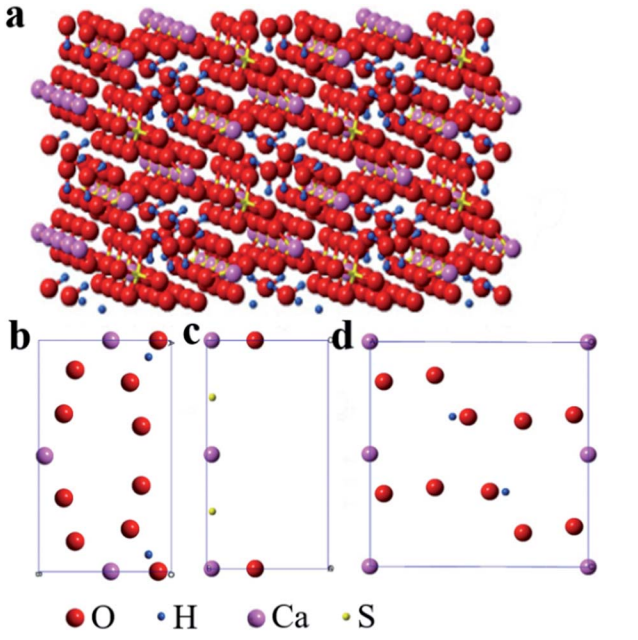

Fig. 6 Molecular model of the obtained rod-shaped α-$CaSO_4 \cdot 0.5H_2O$ crystals (a) 3D model ($2 \times 2 \times 2$ supercell) along the *c*-axis direction and (b–d) facet slice models: (b) (001) and (002), (c) (200) and (400), (d) (020).

Table 1 Distribution of Ca, S, O and H on different facets of the rod-shaped α-$CaSO_4 \cdot 0.5H_2O$ crystals

Facets	Element	Vertex (1/8)	Edge (1/4)	Surface (1/2)	Density/(Å^2)
	Ca	0	3	0	0.0900
(001)	S	0	0	0	0
(002)	O	0	2	8	0.0540
	H	0	0	2	0.0120
	Ca	2	1	0	0.0568
(200)	S	0	0	2	0.0114
(400)	O	0	2	0	0.0057
	H	0	0	0	0
(020)	Ca	4	2	0	0.0066
	S	0	0	0	0
	O	0	0	10	0.0328
	H	0	0	2	0.0066

as a crystal modifier could effectively tune the aspect ratio of the rod-shaped α-$CaSO_4 \cdot 0.5H_2O$ crystals in H_2O.

4 Conclusions

Summary, we have developed a simple and eco-friendly strategy for the synthesis of rod-shaped α-$CaSO_4 \cdot 0.5H_2O$ crystals having a tunable aspect ratio from the industrial phosphogypsum in potassium tartrate aqueous solution. The selective use of potassium tartrate was demonstrated to be vital for the formation of rod-shaped α-$CaSO_4 \cdot 0.5H_2O$ crystals. Once the potassium tartrate was present, the industrial phosphogypsum could be successfully converted into rod-shaped α-$CaSO_4 \cdot 0.5H_2O$ crystals at a lower temperature. As the potassium tartrate concentration increased from 20 mM to 200 mM, the crystals length decreased from 105 μm to 21 μm, and corresponding aspect ratio decreased sharply from 52 : 1 to 1 : 1. The process of the formation of the rod-shaped α-$CaSO_4 \cdot 0.5H_2O$ crystals was explored and discussed, where it started from the dissolution of the $CaSO_4 \cdot 2H_2O$ crystals and the initial form of small particles, then gradually grew into short rod-shaped crystals and finally lead to the uniform rod-shaped α-$CaSO_4 \cdot 0.5H_2O$ crystals. The preferential adsorption of tartrate ions on the top facets of α-$CaSO_4 \cdot 0.5H_2O$ crystals as (001) and (002) inhibit the growth of the crystal along the *c*-axis, and thereby realized the regulation of α-$CaSO_4 \cdot 0.5H_2O$ crystals aspect ratio. We expect our study will provide a new idea for the recycling of industrial phosphogypsum.

Conflicts of interest

There are no conflicts to declare.

Acknowledgements

This work is financially supported by Natural Science Foundation of China (21806065) and Doctoral Special Research Foundation of HFUT (JZ2018HGBZ0122 and JZ2018HGBZ0087). We also thank the support from Anhui Province Key Laboratory of Advanced Catalytic Materials and Reaction Engineering (45000-411104/007) and Anhui Liuguo Chemical Co. Ltd (W2018JSKF0563).

References

1 P. M. Rutherford, M. J. Dudas and R. A. Samek, *Sci. Total Environ.*, 1994, **149**, 1–38.
2 T. Hanan, C. Mohamed, F. A. López, F. J. Alguacil and L. D. Aurora, *J. Environ. Manage.*, 2009, **90**, 2377–2386.
3 C. R. Cánovas, F. Macías, R. Pérez-López, M. D. Basallote and R. Millán-Becerro, *J. Cleaner Prod.*, 2018, **174**, 678–690.
4 Q. S. Chen, C. Y. Jia, Y. Li, J. Xu, B. H. Guan and M. Z. Yates, *Langmuir*, 2017, **33**, 2362–2369.
5 G. M. Jiang, W. Y. Fu, Y. Z. Wang, X. Y. Liu, Y. X. Zhang, F. Dong, Z. Y. Zhang, X. M. Zhang, Y. M. Huang, S. Zhang and X. S. Lv, *Environ. Sci. Technol.*, 2017, **51**, 10519–10525.
6 G. M. Jiang, J. X. Li, Y. L. Nie, S. Zhang, F. Dong, B. H. Guan and X. S. Lv, *Environ. Sci. Technol.*, 2016, **50**, 7650–7657.
7 H. L. Fu, C. Y. Jia, Q. S. Chen, X. T. Cao and X. M. Zhang, *Particuology*, 2018, **40**, 98–104.
8 F. Hao, X. F. Song, T. J. Liu, Y. X. Xu and J. G. Yu, *J. Cryst. Growth*, 2018, **495**, 29–36.
9 S. C. Hou, J. Wang, X. X. Wang, H. Y. Chen and L. Xiang, *Langmuir*, 2014, **30**, 9804–9810.
10 W. P. Zhao, C. H. Gao, G. Y. Zhang, J. Xu, C. X. Wang and Y. M. Wu, *New J. Chem.*, 2016, **40**, 3104–3108.
11 C. Y. Jia, Q. S. Chen, Z. Xu, W. Hao, G. M. Jiang and B. H. Guan, *Ind. Eng. Chem. Res.*, 2016, **55**, 9189–9194.
12 Q. J. Guan, Y. H. Hu, H. H. Tang, W. Sun and Z. Y. Gao, *J. Colloid Interface Sci.*, 2018, **530**, 292–301.
13 H. L. Fu, B. H. Guan and Z. B. Wu, *Fuel*, 2015, **150**, 602–608.
14 J. W. Mao, G. M. Jiang, Q. S. Chen and B. H. Guan, *Colloids Surf., A*, 2014, **443**, 265–271.
15 K. Bao, B. H. Guan, M. Z. Yates and Z. B. Wu, *Langmuir*, 2012, **28**, 14137–14142.
16 Z. Y. Pan, Y. Lou, G. Y. Yang, X. Ni, M. C. Chen, H. Z. Xu, X. G. Miao, J. L. Liu, C. F. Hu and Q. Huang, *Ceram. Int.*, 2013, **39**, 5495–5502.
17 B. H. Guan, G. M. Jiang, H. L. Fu, Y. Li and Z. B. Wu, *Ind. Eng. Chem. Res.*, 2011, **50**, 13561–13567.
18 X. L. Mao, X. F. Song, G. M. Lu, Y. Z. Sun, Y. X. Xu and J. G. Yu, *Ind. Eng. Chem. Res.*, 2014, **53**, 17625–17635.
19 Y. B. Tang and J. M. Gao, *Langmuir*, 2017, **33**, 9637–9644.
20 W. L. Teng, J. S. Wang, J. S. Wu, Y. C. Du, X. J. Jia, H. Y. Li and T. N. Wang, *J. Cryst. Growth*, 2018, **496**, 24–30.
21 L. C. Yang, Z. B. Wu, B. H. Guan, H. L. Fu and Q. Q. Ye, *J. Cryst. Growth*, 2009, **311**, 4518–4524.
22 B. H. Guan, H. L. Fu, Y. Jie, G. M. Jiang, K. Bao and Z. B. Wu, *Fuel*, 2011, **90**, 36–41.
23 L. C. Yang, B. H. Guan, Z. B. Wu and X. F. Ma, *Ind. Eng. Chem. Res.*, 2009, **48**, 7773–7779.
24 Q. J. Guan, H. H. Tang, W. Sun, Y. H. Hu and Z. G. Yin, *Ind. Eng. Chem. Res.*, 2017, **56**, 9831–9838.
25 T. Kamimura, S. Hara, H. Miyuki, M. Yamashita and H. Uchida, *Corros. Sci.*, 2006, **48**, 2799–2812.
26 X. L. Mao, X. F. Song, G. M. Lu, Y. Z. Sun, Y. X. Xu and J. G. Yu, *Ind. Eng. Chem. Res.*, 2015, **54**, 2781–4787.

27 X. L. Mao, X. F. Song, G. M. Lu, Y. X. Xu, Y. Z. Sun and J. G. Yu, *Chem. Eng. J.*, 2015, **278**, 320–327.
28 S. Grudén, M. Sandelin, V. Rasanen, P. Micke, M. Hedeland, N. Axén and M. Jeansson, *Eur. J. Pharm. Biopharm.*, 2017, **114**, 186–193.
29 Z. X. Zhou, F. Buchanan, C. Mitchell and N. Dunne, *Mater. Sci. Eng., C*, 2014, **38**, 1–10.
30 Y. Shen, S. Z. Yang, J. L. Liu, H. Z. Xu, Z. L. Shi, Z. Q. Lin, X. Z. Ying, P. Guo, T. Lin, S. G. Yan, Q. Huang and L. Peng, *ACS Appl. Mater. Interfaces*, 2014, **6**, 12177–12188.
31 D. Pförringer, N. Harrasser, M. Beirer, M. Crönlein, A. Stemberger, M. V. Griensven, M. Lucke, R. Burgkart and A. Obermeier, *Materials*, 2018, **11**, 935–943.
32 C. C. Chen, C. W. Wang, N. S. Hsueh and S. J. Ding, *J. Alloys Compd.*, 2014, **585**, 25–31.
33 H. L. Tan, S. B. Yang, P. Y. Dai, W. Y. Li and B. Yue, *Int. J. Nanomed.*, 2015, **10**, 4341–4350.
34 S. P. Zhang, X. X. Xu, S. A. Memon, Z. J. Dong, D. X. Li and H. Z. Cui, *Constr. Build. Mater.*, 2018, **167**, 253–262.
35 N. Li, L. L. Xu, R. Wang, L. Li and P. M. Wang, *Cem. Concr. Res.*, 2018, **108**, 103–115.
36 X. M. Chen, J. M. Gao, C. B. Liu and Y. S. Zhao, *Constr. Build. Mater.*, 2018, **190**, 53–64.
37 V. Antunes, A. Candeias, M. J. Oliveira, M. Lorena, A. I. Seruya, M. L. Carvalho, M. Gil, J. Mirão, J. Coroado and V. Gomes, *Microchem. J.*, 2016, **125**, 290–298.
38 K. H. Lee and K. H. Yang, *Constr. Build. Mater.*, 2016, **127**, 442–449.
39 A. Farzadi, V. Waran, M. Solati-Hashjin, Z. A. A. Rahman, M. Asadi and N. A. A. Osman, *Ceram. Int.*, 2015, **41**, 8320–8330.
40 C. J. Liu, Q. Zhao, Y. G. Wang, P. Y. Shi and M. F. Jiang, *Appl. Surf. Sci.*, 2016, **360**, 263–269.
41 B. G. Ma, W. D. Lu, Y. Su, Y. B. Li, C. Gao and X. Y. He, *J. Cleaner Prod.*, 2018, **195**, 396–405.
42 G. M. Jiang, H. Wang, Q. S. Chen, X. M. Zhang, Z. B. Wu and B. H. Guan, *Fuel*, 2016, **174**, 235–241.
43 Y. Q. Zhang, D. Wang, L. L. Zhang, Y. Le, J. X. Wang and J. F. Chen, *Ind. Eng. Chem. Res.*, 2017, **56**, 14053–14059.
44 G. M. Jiang, Q. S. Chen, C. Y. Jia, S. Zhang, Z. B. Wu and B. H. Guan, *Phys. Chem. Chem. Phys.*, 2015, **17**, 11509–11515.
45 F. Li, J. L. Liu, G. Y. Yang, Z. Y. Pan, X. Ni, H. Z. Xu and Q. Huang, *J. Cryst. Growth*, 2013, **374**, 31–36.
46 K. Gupta, S. Singh and M. S. R. Rao, *Cryst. Growth Des.*, 2016, **16**, 3256–3261.
47 K. Park, J. M. B. Evans and A. S. Myerson, *Cryst. Growth Des.*, 2003, **6**, 991–995.
48 J. M. Ouyang, H. Zheng and S. P. Deng, *J. Cryst. Growth*, 2006, **293**, 118–123.
49 Y. T. Song, P. J. Swedlund, C. W. Zou and R. D. Hamid, *Chem. Geol.*, 2013, **347**, 114–122.
50 G. F. Moreira, E. R. Peçanha, M. B. M. Monte, L. S. L. Filho and F. Stavale, *Miner. Eng.*, 2017, **110**, 96–103.
51 Y. Song, D. Zemlyanov, X. Chen, H. C. Nie, Z. Y. Su, K. Fang, X. H. Yang, D. Smith, S. Byrn and J. W. Lubach, *Mol. Pharmaceutics*, 2015, **13**, 483–492.
52 L. O. Filippov, V. V. Severov and I. V. Filippova, *Int. J. Miner. Process.*, 2013, **123**, 120–128.
53 W. Kai, Y. N. Qin, L. Fan, M. Q. Li, L. Qiao, L. Fei, J. R. Feng, Y. Chao, G. Peng and S. J. Guo, *Small Methods*, 2018, **2**, 1700331–1700339.
54 C. Y. Tang, N. Zhang, Q. Shao, X. Q. Huang and X. H. Xiao, *Nanoscale*, 2019, **12**, 5145–5150.
55 *Material Studio 5.0*, Molecular Simulations Inc. (MSI), Genetics Computer Group (GCG), Synopsys Scientific and Oxford Molecular Group (OMG), 2009.